ADVANCED MATERIALS
www.advmat.de

Active Diffusion Controlled Dual Stability in Thermoelectrics for Sustainable Heat Harvesting

*Longquan Wang, Airan Li, Xinzhi Wu, Jiankang Li, Takeo Ohsawa, and Takao Mori**

Thermoelectric technology offers a promising pathway toward global sustainability by harvesting waste heat. However, long-term stability is hindered by inevitable elemental diffusion, degrading both the thermoelectric junction and material properties, which prevents the realization of power generation applications. Here, dual and superior stability is achieved in high-performance $Mg_3(Bi,Sb)_2$, surpassing prior studies that focus on either junction or material stability. By introducing an Mg layer at the junction, detrimental Mg diffusion is suppressed and compensate for Mg loss in the material, effectively stabilizing both junctions and materials for over 100 days. As a result, a thermoelectric module with 30-day-aged $Mg_3(Bi,Sb)_2$ is able to maintain an outstanding power density of 0.45 W cm^{-2} and remarkable conversion efficiency of 8.6%, demonstrating unprecedented stability. These findings provide new insights into thermoelectric junction engineering, shifting from interface optimization to comprehensive stabilization, advancing the practical viability of thermoelectric energy harvesting for renewable and waste heat applications.

1. Introduction

The transition from centralized fossil fuel systems to renewable and sustainable technologies aligns with the United Nations Sustainable Development Goals.[1,2] However, all thermodynamic processes inevitably produce heat loss due to the irreversibility of the Carnot heat engine. Globally, an estimated 200 exajoules (EJ) of low-grade waste heat are dissipated annually,[1] representing an untapped energy source. Converting this environmental waste heat into usable energy with eco-friendly and sustainable technologies has become a critical focus in the pursuit of a sustainable future. Thermoelectric (TE) devices offer a promising solution by converting thermal gradients into electricity through the movement of charge carriers driven by heat.[3,4] TE devices enable direct energy conversion from waste heat to electricity with minimal maintenance requirements, supporting a sustainable energy supply.[5,6] Despite significant progress in TE materials research, maintaining long-term high efficiency in TE devices remains a serious challenge for implementation due to performance deterioration after elemental diffusion during operation.

TE devices rely on both TE materials and interface materials (TEiMs) for efficient power generation.[7–9] Recent advancements have unveiled high-performance TE materials, particularly near-room-temperature materials intended to replace Bi_2Te_3, such as $Mg_3(Bi,Sb)_2$,[10–21] MgAgSb,[22–25] and Ag_2Q (Q = Te, Se, S).[26–29] At the same time, designing reliable TEiMs is equally crucial, as they minimize electrical and thermal resistance at interfaces. Effective screening strategies, such as phase diagram calculations,[9,30,31] alloying,[32,33] interfacial reaction and diffusion criteria,[34,35] and high-throughput methods,[36,37] have identified TEiMs with low contact resistivity (ρ_c). Despite these advancements, elemental diffusion at interfaces remains a persistent challenge, progressively degrading both the TE material and its interface. Since diffusion is fundamentally driven by thermodynamic equilibrium, it cannot be completely suppressed, making long-term stability a critical yet unresolved issue.

Traditional approaches primarily focus on minimizing ρ_c to improve TE junction performance, assuming that stability issues arise solely from interfacial degradation. However, even junctions with initially low ρ_c suffer from diffusion-driven degradation,[38] particularly in composition-sensitive TE materials,[39] where even minor elemental migration can drastically alter the transport properties of materials. For instance, in Bi_2Te_3-based materials, a minor shift in the Te mole fraction from 0.5997 to 0.6002 can induce a transition from p-type to n-type conduction due to native defect evolution.[40] Similarly, in PbTe, interfacial diffusion perturbs the delicate balance

L. Wang, A. Li, X. Wu, J. Li, T. Mori
Research Center for Materials Nanoarchitectonics (MANA)
National Institute for Materials Science (NIMS)
Namiki 1-1, Tsukuba 305-0044, Japan
E-mail: MORI.Takao@nims.go.jp
J. Li, T. Mori
Graduate School of Pure and Applied Sciences
University of Tsukuba
Tennodai 1-1-1, Tsukuba 305–8671, Japan
T. Ohsawa
Research Center for Electronic and Optical Materials
National Institute for Materials Science (NIMS)
Namiki 1-1, Tsukuba 305-0044, Japan

The ORCID identification number(s) for the author(s) of this article can be found under https://doi.org/10.1002/adma.202508270

DOI: 10.1002/adma.202508270

between Pb-rich and Te-rich states,[41] affecting chemical potential and doping efficiency. The issue is even more pronounced in $Mg_3(Bi,Sb)_2$-based materials, where the high chemical reactivity and volatility of Mg exacerbate instability. In n-type $Mg_3(Bi,Sb)_2$, excess Mg modifies the chemical potential and suppresses Mg vacancy formation,[10,42] enabling n-type transport. However, uncontrolled Mg migration at the interface can rapidly degrade material properties or even trigger a conduction-type reversal from n-type to p-type, fundamentally altering device performance.

N-type $Mg_3(Bi,Sb)_2$ has emerged as a leading candidate for low-temperature thermal energy harvesting due to its high TE performance, earth-abundant composition, and excellent mechanical toughness.[43–45] Despite achieving high dimensionless figure-of-merit (zT) values of ≈1.0 at room temperature and ≈2.0 at elevated temperatures,[18,46–49] practical application is severely limited by chemical instability and thermal instability.[50–52] Continuous Mg reaction and evaporation leads to performance degradation, a challenge further exacerbated at TE junctions, where interfacial diffusion accelerates instability beyond that observed in bulk materials. As a result, achieving sustainable TE power generation requires a holistic approach that stabilizes both the materials and its interface—an issue that remains largely unsolved.

To mitigate these limitations, various metals such as Fe,[16,53–55] Ni,[13,56] and Nb,[36] were explored as TEiMs in $Mg_3(Bi,Sb)_2$ junctions. However, a sharp increase in ρ_c after aging indicates significant interfacial diffusion or reaction, primarily driven by the highly reactive nature of Mg. Even slight Mg migration at the interface can degrade material performance.[42] To counteract these effects, alloy-based TEiMs have been developed, including 304 stainless steel (304SS),[57] Cu_7Ni_3,[58] Fe_7Mg_2Cr,[32] $Mg_{4.3}Sb_3Ni$,[59] and FeCrTiMnMg,[32] many of which incorporate Mg to mitigate Mg loss from the material matrix. However, conventional TEiMs still exhibit Mg concentration gradients at interfaces, sustaining a chemical potential imbalance that perpetuates diffusion-driven degradation. Material deterioration from interfacial diffusion has been underappreciated, yet it poses a significant barrier to achieving sustainable TE power generation in $Mg_3(Bi,Sb)_2$ systems. The rapid degradation of material properties—exemplified by a shift from n-type to p-type conductivity when Fe is used as a contact layer—[60]highlights the urgent need for dual stability in both materials and interfaces.

To address the long-standing stability challenges in $Mg_3(Bi,Sb)_2$, we introduce an Mg interlayer between $Mg_3(Bi,Sb)_2$ and the metallization layer to actively control the Mg diffusion. This interlayer effectively prevents Mg loss into the contact layer while compensating for Mg depletion at grain boundaries, ensuring dual stability in both ρ_c and material performance. As a result, the junction maintains holistic stability for over 100 days at 573K. Even after 30 days of aging, TE modules incorporating this dual-stable $Mg_3(Bi,Sb)_2$ junction achieve a remarkable conversion efficiency of 8.6% and a power density of 0.45 W cm^{-2} under a relatively small 294 K temperature gradient. These results highlight the promising potential of a dual-stable $Mg_3(Bi,Sb)_2$ junction for sustainable low-grade heat harvesting. Furthermore, this strategy can be extended to other TE materials sensitive to chemical potential variations, providing a generalizable solution for enhancing the performance and longevity of TE devices.

2. Results

2.1. Achievement of Dual Stability in $Mg_3(Bi,Sb)_2$ Junctions

Conventional TEiMs often exhibit Mg concentration gradients at interfaces (**Figure 1a**), which drive diffusion due to differences in chemical potential. This diffusion undermines the stability of the interfaces and leads to Mg loss, significantly impacting the TE properties of materials. In some cases, such as with Fe as the TEiM, this diffusion can even cause a transition in conduction type from n- to p-type in $Mg_3(Bi,Sb)_2$ junctions.[60] In contrast, inserting an Mg interlayer creates a concentration barrier that effectively suppresses Mg diffusion into the TEiM, while also compensating for Mg loss in the material. This dual mechanism stabilizes both the junction interface and the TE material.

To verify this effect, we fabricated $Mg/Mg_3(Bi,Sb)_2$ junctions and analyzed their thermal stability over extended periods. Linear resistance scanning across the junction after aging at 573 K reveals a stable resistance trend, indicating holistic stability of the junction (Figure 1b). The unchanged slope of the linear resistance curve in the material region confirms stable transport properties. Evaluating stability at 573 K is directly relevant to real-world operating conditions for low-grade waste heat harvesting. In addition, the negligible resistance jump at the interface suggests a consistently low ρ_c, which remains unaffected by aging. In contrast, conventional TEiMs typically exhibit a decline in σ over time. This deterioration is primarily caused by Mg diffusion from the material to the contact layer, with the concentration gradient at the interface accelerating this process. Notably, our Mg diffusion barrier is the first TEiM to maintain undeteriorated material performance in $Mg_3(Bi,Sb)_2$ junctions, achieving superior stability compared to other TEiMs, and even outperforming coating-based stabilization methods (Figure 1c).[33] This enhanced stability can be attributed to the effective prevention of Mg loss and the compensatory role of the interlayer, as will be discussed later. Consequently, the $Mg/Mg_3(Bi,Sb)_2$ junction maintains stable material properties for over 50 days at 573 K, outperforming other junctions.

Achieving a low ρ_c is also critical for optimizing TEiMs, as high ρ_c impairs device performance. The power density and conversion efficiency of TE devices are significantly impacted by ρ_c, as described by the equation:[8]

$$ZT_D = zT_M \times L/(L + 2\rho_c \times \sigma) \quad (1)$$

where L, ρ_c, σ, zT_M, ZT_D are the length of TE legs, contact resistivity, electrical conductivity, and the zT of materials and devices, respectively. For instance, to limit a 5% loss in ZT_D/zT_M for a device with $L = 2$ mm and $\sigma = 10^5$ S m^{-1}, ρ_c must remain below 5 μΩ cm^2. As shown in Figure 1d, previously reported junctions exhibit a significant increase in ρ_c over time,[32,33,36,57,60,61] primarily due to elemental diffusion at the interfaces. This rapid increase in ρ_c compromises the efficiency of the TE devices during operation. In contrast, the $Mg/Mg_3(Bi,Sb)_2$ junction demonstrated exceptional stability, maintaining a low ρ_c (<5 μΩ·cm^2) over 30 days of aging. The Mg interlayer effectively blocks elemental migration, preserves interface integrity, and ensures reliable long-term performance. Overall, the developed $Mg/Mg_3(Bi,Sb)_2$ junction exhibits distinct advantages over conventional designs, achieving

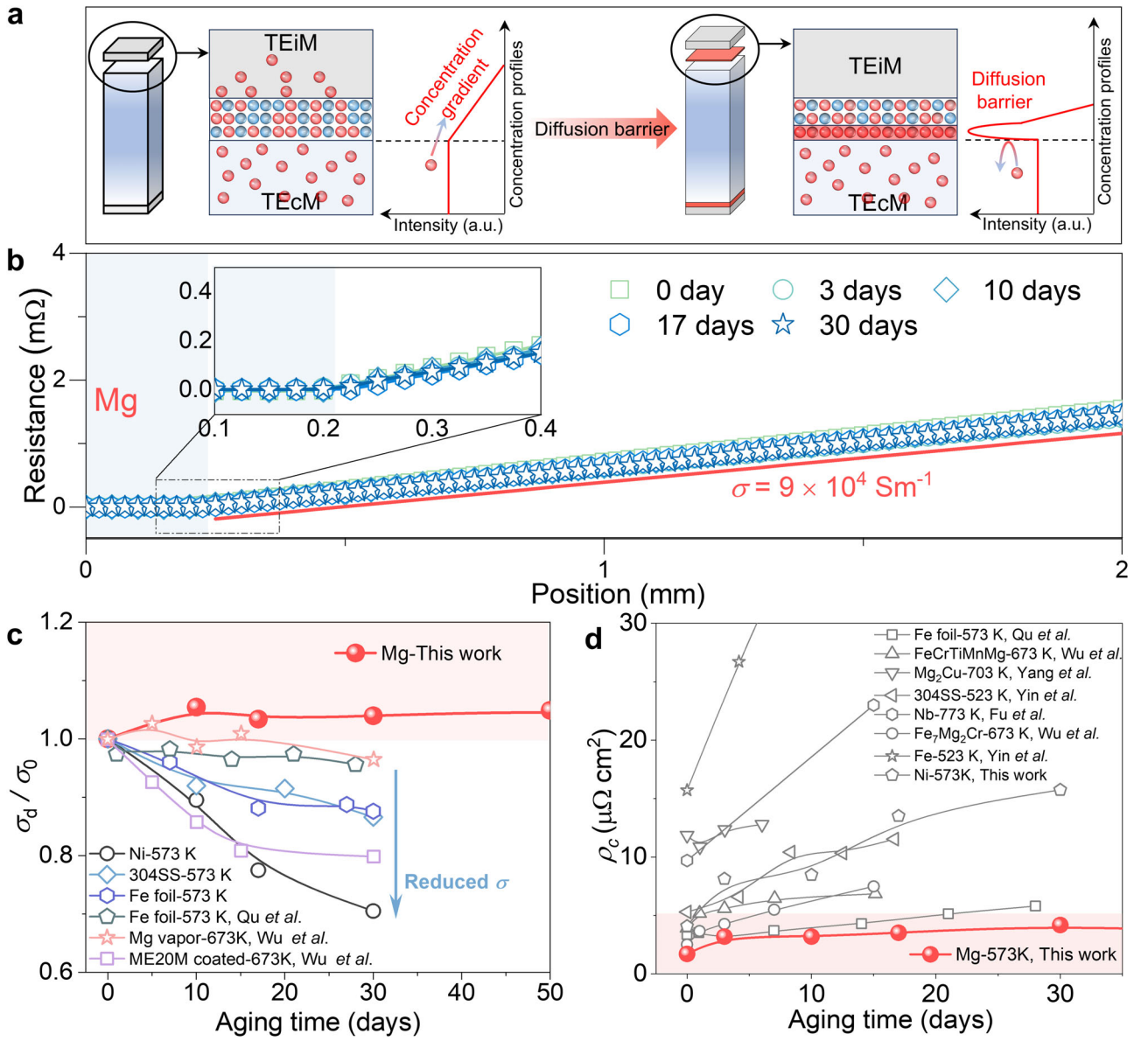

Figure 1. Achievement of overall stability in TE junctions. a) Comparison between conventional TEiMs and Mg interlayer, highlighting the distinct Mg concentration gradients at the interface. b) Evolution of linear resistance scanning across the $Mg/Mg_3(Bi,Sb)_2$ junction after aging at 573 K. c) Comparison of the σ_d/σ_0 for materials in TE junctions,[33,60] where σ_0 is initial σ and σ_d is the σ after aging. d) Comparison of the evolution of ρ_c over time.[32,33,36,57,60,61]

dual stability in both ρ_c and material performance by actively controlling the Mg diffusion at the interface.

2.2. Superior Stability of TE Materials in TE Junctions

In $Mg_3(Bi,Sb)_2$ materials, the potential diffusion and loss of Mg hinder performance stability by introducing Mg vacancies. The high saturated vapor pressure and volatility of Mg lead to significant diffusion during the sintering process of the junction, causing disrupted composition uniformity in $Mg_3(Bi,Sb)_2$. This phenomenon is evident from the poor linearity in the contact resistance curves observed in junctions with commonly used TEiMs such as Fe and Ni (Figure S1, Supporting Information).[60] Mg loss also introduces strong compositional fluctuations in $Mg_3(Bi,Sb)_2$,[62] hindering the achievement of high TE performance. In contrast, the $Mg/Mg_3(Bi,Sb)_2$ joint demonstrates perfect linearity in the contact resistance curve (Figure S2, Supporting Information), indicating suppressed Mg loss during the sintering process and preserved composition homogeneity. Moreover, continuous Mg diffusion occurs in conventional junctions with a concentration gradient during the aging process, as evidenced by the progressively changing slopes of contact resistance curves. These changes indicate deteriorating σ, as observed in the $Ni/Mg_3(Bi,Sb)_2$ and $304SS/Mg_3(Bi,Sb)_2$ junctions (**Figure 2a**). In contrast, the $Mg/Mg_3(Bi,Sb)_2$ junction exhibits

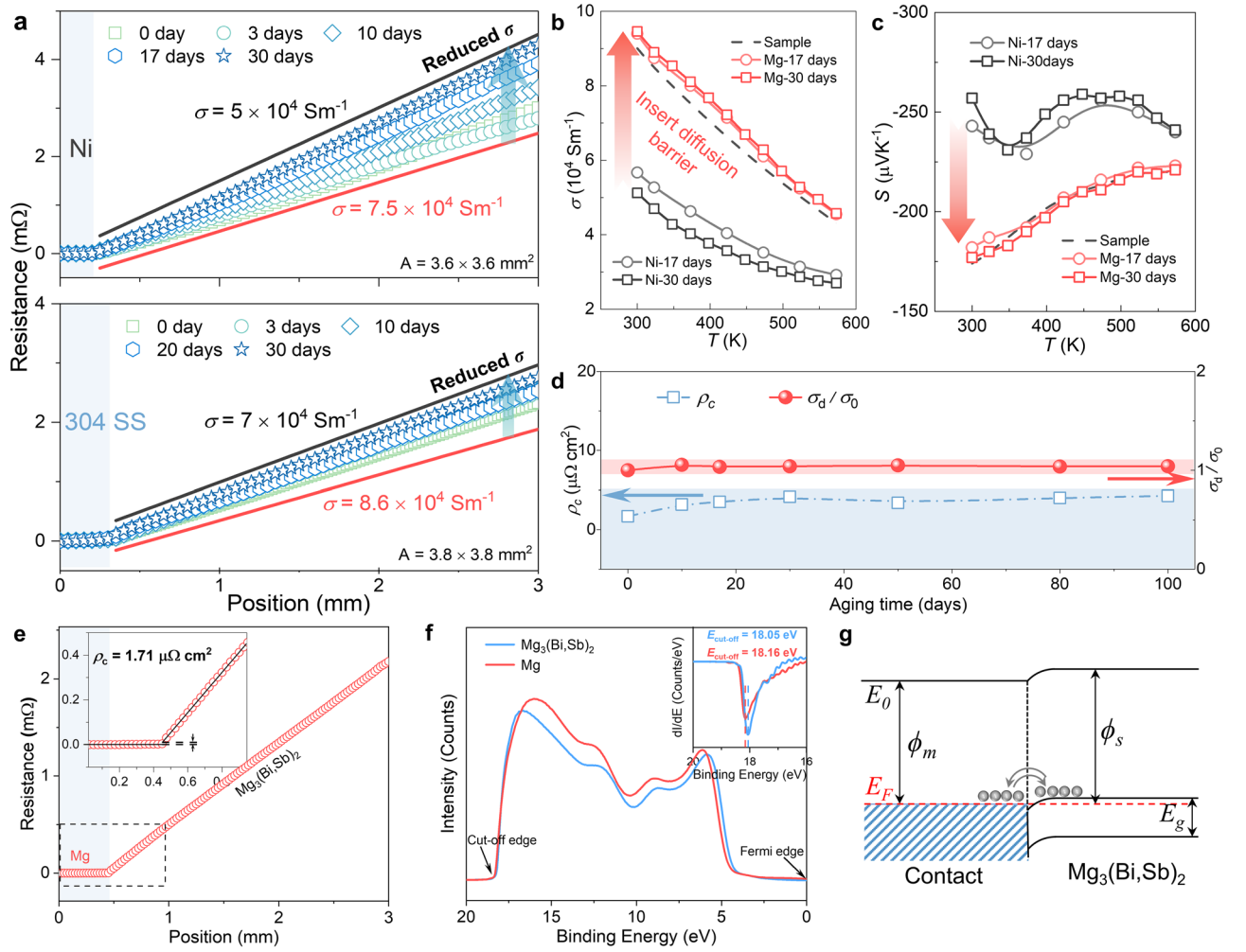

Figure 2. Dual stability of material properties and ρ_c. a) Evolution of linear resistance scanning across junctions after aging at 573 K. Temperature-dependent b) σ, c) Seebeck coefficient of materials in different junctions. d) Evolution of ρ_c and σ of the TE material in the Mg/$Mg_3(Bi,Sb)_2$ junction over aging time at 573 K. e) Room-temperature ρ_c of the Mg/$Mg_3(Bi,Sb)_2$ interface. f) UPS spectrum of $Mg_3(Bi,Sb)_2$ and Mg. g) Schematic illustration of carrier transport at the ohmic contact interface.

steady linearity in the contact resistance curves (Figure 1b), suggesting excellent thermal stability. Previous studies have demonstrated that dense Fe foil can effectively mitigate Mg diffusion from the material matrix to the interfacial layer.[60] However, the gradual increase in contact resistance after aging indicates that Mg diffusion still occurs due to the concentration gradient (Figure S3, Supporting Information).[63,64] In comparison, the developed Mg/$Mg_3(Bi,Sb)_2$ junction displays superior thermal stability relative to other TEiMs used in $Mg_3(Bi,Sb)_2$, including Ni, 304 stainless steel (304SS), and Fe foil.

Furthermore, the electrical transport properties of the aged TE junctions were investigated to evaluate material stability. The σ of materials in Ni/$Mg_3(Bi,Sb)_2$ junctions significantly decreases across the entire temperature range compared to the pristine sample, with this trend intensifying as aging time increases (Figure 2b). Specifically, the room-temperature σ of the Ni/$Mg_3(Bi,Sb)_2$ junction drops to 5.1×10^4 S m^{-1}, a 43% reduction compared to the pristine sample (9×10^4 S m^{-1}). This decline is related to Mg diffusion from the material into the interface layer. However, after incorporating a Mg diffusion barrier, the σ remains stable over extended aging periods and even slightly exceeds that of the pristine sample. This stability suggests that Mg diffusion to the interface layers has been effectively blocked and that potential Mg compensation from the Mg layer optimizes the material's electrical transport properties. The slight initial increase in σ observed during early-stage aging is likely due to improved compositional homogeneity and reduced grain-boundary potential (Figure 1c).[62]

A similar trend is observed in the Seebeck coefficient, as shown in Figure 2c. The sharply increased Seebeck coefficient in the Ni/$Mg_3(Bi,Sb)_2$ junctions indicates reduced carrier concentration, driven by Mg loss. According to phase boundary mapping,[42] excess Mg is critical for maintaining n-type behavior in $Mg_3(Bi,Sb)_2$ and significantly impacts carrier concentration. The observed material deterioration has a much stronger impact on TE device performance than ρ_c. For example, even when ρ_c increases to 20 μΩ cm^2 in junctions with dimensions of $3.8 \times 3.8 \times 6$ mm^3, the internal resistance contribution from

two joints amounts for only ≈6.4% of the total, far lower than the performance loss caused by material deterioration (over 40% in Ni/$Mg_3(Bi,Sb)_2$ junctions). After aging at 573 K for 30 days, all tested junctions (Ni, 304SS, and Fe foil) show reductions in σ of over 10%, except for the Mg/$Mg_3(Bi,Sb)_2$ junction (Figure 1c). To ensure the reliability of these results, we cross-validated the σ values obtained from linear resistance scanning with those measured using a standard four-probe method on a ZEM-3 system (Figure S4, Supporting Information), confirming consistency within 5% error.

2.3. Simultaneously High Stability of Contact in Mg/$Mg_3(Bi,Sb)_2$ Junctions

The ρ_c in a metal-semiconductor contact depends on the barrier height (ϕ_B) and carrier concentration (n), described by the relationship: $\rho_c \sim \exp(q\phi_B/n^{1/2})$,[8] where q is the elementary charge. In other junctions, Mg diffusion reduces carrier concentration, leading to an increase in ρ_c over time (Figure 1d). Consequently, blocking Mg diffusion from the material into the interface layers is crucial, not only for maintaining the thermal stability of materials but also for ensuring a low ρ_c. Remarkably, the Mg/$Mg_3(Bi,Sb)_2$ junction maintained an ultra-low ρ_c (<5 μΩ cm^2) and stable material performance, including undeteriorated σ, over 100 days of aging at 573 K (Figure 2d). This underscores the critical importance of controlling Mg diffusion when fabricating reliable TE junctions. The aging duration of 100 days at 573 K is significantly longer than most reported studies on TE junction stability, and this stability is expected to extend beyond 100 days, as suggested by the absence of degradation in electrical performance and the overall robustness of the interface design.

In our Mg/$Mg_3(Bi,Sb)_2$ junctions, an ultra-low ρ_c of 1.71 μΩ cm^2 was achieved (Figure 2e), which is the lowest value reported to date (Figure S5, Supporting Information). This result represents the simplicity of module fabrication using metal contacts instead of alloy contacts. To explore the origin of the low ρ_c, the barrier height related to the work function (ϕ) of the metal-semiconductor contact was investigated.[65,66] For a contact between an n-type semiconductor and a metal, achieving an Ohmic contact is essential to minimize ρ_c.[35] In such cases, the work function of the semiconductor (ϕ_s) should be greater than that of the metal (ϕ_m). The work functions were calculated using the equation:

$$\phi = h\nu - \left(E_{cutoff} - E_{Fermi}\right) \quad (2)$$

where h, ν, E_{cutoff} and E_{Fermi} are Plank constant, the frequency of the excited photons, the energy of the cut-off edge, and the energy of the Fermi edge, respectively. Ultraviolet photoelectron spectroscopy (UPS) measurements were conducted to determine E_{cutoff}, with the photon energy ($h\nu$) set to 21.22 eV. The measured E_{cutoff} values for $Mg_3(Bi,Sb)_2$ and Mg were 18.05 and 18.16 eV, respectively (Figure 2f). Accordingly, the calculated work functions were 3.17 eV for $Mg_3(Bi,Sb)_2$ and 3.06 eV for Mg. Since $\phi_s > \phi_m$, an Ohmic contact is expected to form at the interface of the junction. This expectation is further supported by the linear I–V characteristics, with no rectification observed even after 30 days of aging (Figure S6, Supporting Information).

At the Mg/$Mg_3(Bi,Sb)_2$ interface, electrons transfer from the Mg layer into $Mg_3(Bi,Sb)_2$ due to Fermi level alignment,[65,66] reaching equilibrium through charge redistribution. This charge transfer induces an electron accumulation region on the $Mg_3(Bi,Sb)_2$ side, increasing the local electron concentration and enhancing conductivity. The favorable band alignment at the Mg/$Mg_3(Bi,Sb)_2$ junction ensures barrier-free electron transport, enabling an Ohmic contact (Figure 2g).[8,65] These characteristics collectively account for the observed low ρ_c in the Mg/$Mg_3(Bi,Sb)_2$ junction. However, despite the formation of an Ohmic contact, a small yet nonzero ρ_c is still observed. This residual ρ_c likely originates from interface roughness, potential interfacial impurities (e.g., thin oxide layers), and localized variations in chemical composition, which may introduce minor scattering effects. Nevertheless, the measured ρ_c remains significantly lower than that of conventional TE junctions, confirming the superior electrical transport of the Mg/$Mg_3(Bi,Sb)_2$ interface. This ultra-low ρ_c remains stable, owing to the reliable stability of both the contact layer and the TE material properties.

2.4. Blocking Mg Diffusion from Materials to the Contact Layer and Mg Compensation

To uncover the origins of the remarkable stability observed in both ρ_c and material properties, we performed scanning electron microscope (SEM) imaging and energy-dispersive X-ray spectroscopy (EDS) analysis. In the Ni/$Mg_3(Bi,Sb)_2$ junction, a prominent diffusion layer (≈10 μm thick) was observed after sintering (**Figure 3a**), primarily composed of Mg and Ni (Figure S7, Supporting Information). Moreover, significant compositional fluctuations, including Bi-rich phases within the materials, were detected. These compositional fluctuations are associated with Mg loss, which compromises the electrical transport properties of $Mg_3(Bi,Sb)_2$.[62,67] As hypothesized, the diffusion layer expands significantly after aging, increasing in thickness from ≈10 to ≈30 μm (Figure 3b), further degrading the material's performance. This growth was accompanied by the formation of Mg-Ni alloys near the diffusion region, destabilizing the interface (Figure S8, Supporting Information). Even when the TEiM was replaced with an alloy such as 304 stainless steel, Mg diffusion from the material to contact layer persisted (Figure 3c). The mechanism underlying this material deterioration is illustrated in Figure 3d. The concentration gradient drives Mg diffusion, introducing abundant Mg vacancies within $Mg_3(Bi,Sb)_2$, which reduces carrier concentration and σ. Simultaneously, the unstable interface and decreased carrier concentration contribute to increased ρ_c after aging.

Remarkably, the Ni/Mg/$Mg_3(Bi,Sb)_2$ junction exhibits a well-defined interface structure after sintering, with the Mg layer (≈5 μm thick) effectively blocking Mg element from the material into the metallization layer (Figure 3e). Moreover, Ni from the metallization layer diffuses into the Mg layer, forming Mg_2Ni, as confirmed by the phase diagram.[68] This process protects the Mg layer from oxidation and strengthens the bonding at the Ni/Mg interface. EDS analysis further reveals that no matrix elements diffuse into the Ni layer, which remains composed entirely of Ni (Figures S9 and S10, Supporting Information). Notably, this robust sandwich structure remains intact even after extended

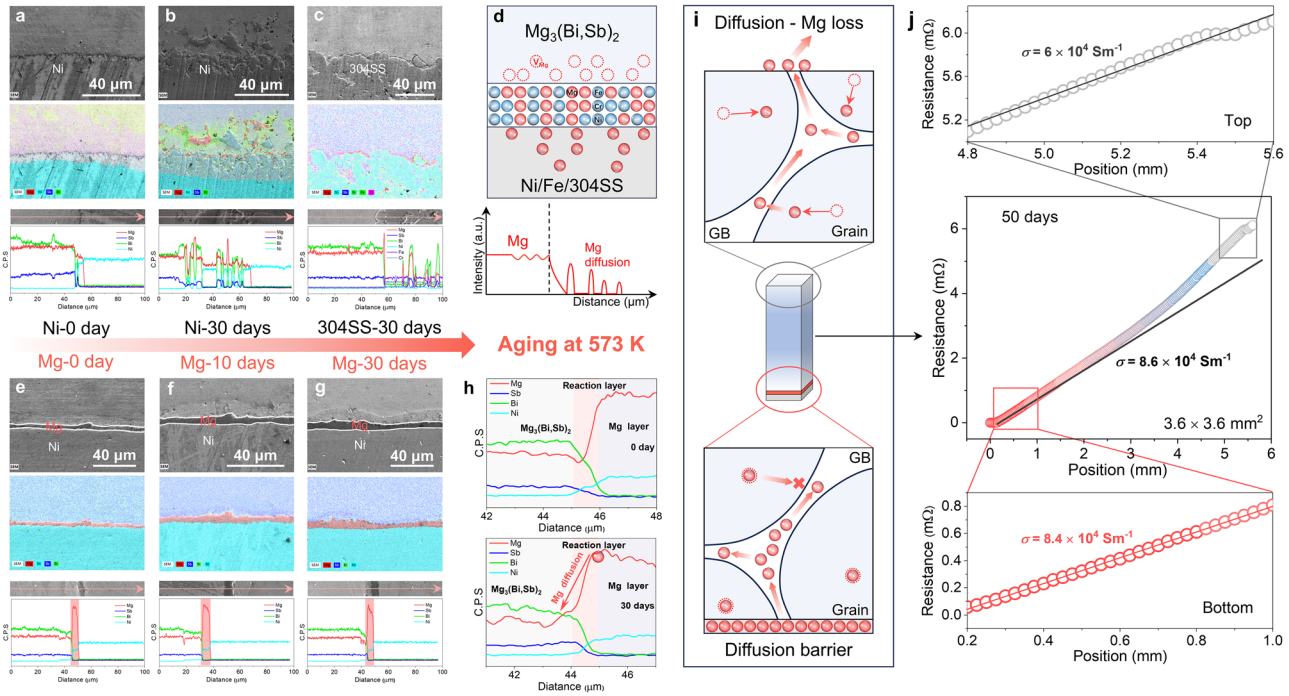

Figure 3. Blocking Mg diffusion and enabling Mg compensation. SEM images, EDS mapping, and line scanning results of different junctions with TEiMs: a) Ni after sintering, b) Ni after aging for 30 days, and c) 304SS after aging for 30 days. d) Schematic illustration of the interface structure following Mg diffusion in conventional junctions. SEM images, EDS mapping, and line scanning results of $Mg/Mg_3(Bi,Sb)_2$ junctions: e) as-sintered (0 days), f) after 10 days of aging, and g) after 30 days of aging. h) Comparison of the composition profile in the $Mg/Mg_3(Bi,Sb)_2$ junction after aging. i) Schematic of Mg diffusion blocking and potential Mg compensation mechanisms at the interface. j) Contact resistance curve of the junction in (i) after aging.

aging (Figure 3f,g), demonstrating excellent thermomechanical stability. Over time, Ni continues to diffuse into the Mg layer, forming additional Mg_2Ni alloys and creating a metallurgically bonded contact that further enhances interfacial strength (Figure S11, Supporting Information). Additionally, a ≈1 μm reaction layer forms at the interface after sintering (Figure 3h), and Mg is known to form strong bonds with $Mg_3(Bi,Sb)_2$,[32] ensuring high shear strength in the $Mg/Mg_3(Bi,Sb)_2$ junction. Even after 30 days of aging at 573 K, no apparent expansion of this reaction layer is observed, further confirming its thermomechanical stability. Importantly, the Mg layer disrupts the concentration gradient driving Mg diffusion into the contact layers while consistently supplying Mg to the TE material. This fully inverted Mg diffusion trend in our $Mg/Mg_3(Bi,Sb)_2$ junction contributes to its unprecedented thermal stability compared to previous studies. However, compared to the pronounced Mg back-diffusion into the TE material, Mg diffusion into the Ni layer is minimal, owing to the dense Ni foil (Figure S11, Supporting Information).

Microstructural characterization sheds light on the mechanisms driving the exceptional thermal stability of materials in the $Mg/Mg_3(Bi,Sb)_2$ junction. A direct comparison between the $Mg/Mg_3(Bi,Sb)_2$ joint and material without a contact layer highlights two key effects of the Mg layer: inhibition of Mg diffusion and Mg compensation. As shown in Figure 3i, when no contact layer is present, the upper side of the junction suffers from significant Mg loss during long-term operation at elevated temperatures. This Mg loss introduces Mg vacancies and hole carriers, adversely impacting TE performance. Thermodynamically, Mg vacancies are more likely to form at grain boundaries than within the bulk phase due to the higher Gibbs free energy at grain boundaries. This grain boundary diffusion mechanism, which has been previously validated,[51,69] contributes to Mg deficiencies at grain boundaries.[70] These deficiencies further propagate into the grains, creating a concentration gradient of Mg from the bulk to the grain boundaries and interfaces, accelerating the Mg loss process.

In contrast, the insertion of an Mg layer establishes an Mg-rich environment at the interface, which is thermodynamically favorable for blocking Mg diffusion pathways. Additionally, Mg compensation from the interface to the grain boundary creates a Mg-enriched grain boundary. This Mg-rich grain boundary effectively suppresses further Mg diffusion from the material bulk to the grain boundary. This Mg compensation is expected to propagate throughout the material via grain boundary diffusion, offsetting surface-evaporation-induced Mg loss and thereby maintaining stable σ across the entire junction (Figure S2, Supporting Information). As a result, grain-boundary potential barriers are significantly reduced, thereby enhancing electron transport in the material. This is supported by the slightly improved σ observed in the $Mg/Mg_3(Bi,Sb)_2$ junction (Figure 2b). Therefore, this Mg compensation effect not only enhances grain-boundary transport by reducing potential barriers but also maintains carrier concentration and suppresses increases in ρ_c during aging.

Long-term thermal stability tests at 573 K demonstrate the effectiveness of the Mg layer. Initially, the junction exhibits perfect linearity in the contact resistance curve and high σ due to the Mg layer's stabilization effects during sintering (Figure S12, Supporting Information). After sintering, the top contact layer was

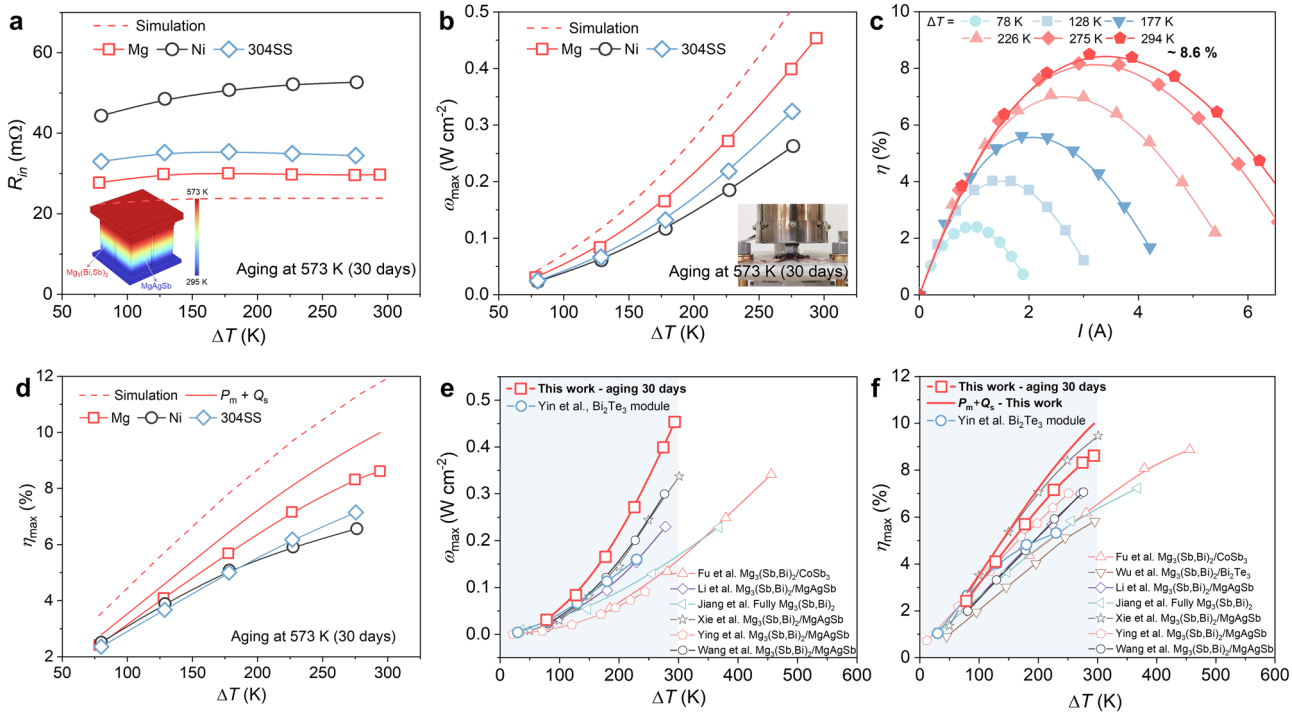

Figure 4. Superior performance of TE module based on Mg/$Mg_3(Bi,Sb)_2$ junctions. Comparison of a) R_{in} and b) ω_{max} among modules fabricated with different junctions. The inset in (a) illustrates the two-pair module design, while the inset in (b) shows optical image of the Mini-PEM system used for TE module performance evaluation. c) η as a function of I under different ΔT. d) Comparison of η_{max} for modules with different junctions. e) ω_{max} and f) η_{max} of the two-pair module in this work compared with previously reported results from the literature.[9,24,33,36,49,53,71,72]

removed by polishing for aging tests. Over time, Mg loss reduces σ, particularly on the top side, where it declines by ≈29% to ≈6×10^4 S m^{-1} after 50 days (Figure 3j). In contrast, the bottom side retains excellent materials stability, maintaining σ at ≈8.4×10^4 S m^{-1}. This highlights the effectiveness of the Mg layer in blocking diffusion and compensating Mg at grain boundaries, ensuring stable chemical potential and performance in materials. This approach ensures unparalleled stability in both material properties and contact, representing a significant step forward in the development of long-lasting $Mg_3(Bi,Sb)_2$-based TE systems. While the Mg interlayer is primarily responsible for suppressing diffusion and stabilizing the junction, the addition of a Ni layer enhances solderability and supports practical device integration.

2.5. Sustainable Power Generation in Modules using Mg/$Mg_3(Bi,Sb)_2$ Junctions

To evaluate the potential of Mg/$Mg_3(Bi,Sb)_2$ junctions for long-term power generation, we fabricated two-pair TE modules, as illustrated in the inset of **Figure** 4a. The p-type MgAgSb was selected for its excellent near-room-temperature TE performance, with the TE properties of $Mg_3(Bi,Sb)_2$ and MgAgSb presented in Figures S13 and S14 (Supporting Information). To minimize the influence of the p-type junctions, Sb-based alloy was used as the contact layer for p-type MgAgSb due to its low ρ_c (Figure S15, Supporting Information).[38] Multiple TE modules were fabricated by using aged n-type junctions (30 days at 573 K), including conventional TEiMs such as Ni and 304SS for direct comparison. Detailed data on output voltage (V), output power (P), heat flow from the cold side (Q_c), and conversion efficiency (η) are presented in Figures S16–S18 (Supporting Information). The linearity of the current (I) versus V relationship enabled determination of the internal resistance (R_{in}) from the slope. The module with Ni as the contact layer exhibited an ultrahigh R_{in}, which cannot be solely attributed to the increased ρ_c (Figure 4a). A significant contribution to the increased R_{in} came from material degradation, as discussed earlier. Using alloy-based contact layers, such as 304SS, partially delayed material deterioration, resulting in reduced R_{in} compared to Ni. However, the R_{in} remained significantly higher than in the module with Mg/$Mg_3(Bi,Sb)_2$ junctions, consistent with prior observations. Our developed active diffusion control, employing an Mg layer, ensures the long-term thermal stability of both the ρ_c and material properties. This results in a markedly lower R_{in} in modules with Mg/$Mg_3(Bi,Sb)_2$ junctions, where $R_{in} = R_{contacts} + R_{materials}$. This improvement highlights the critical role of the Mg layer in achieving enhanced performance and durability in TE modules. Benefiting from the significantly lower R_{in}, the module with Mg/$Mg_3(Bi,Sb)_2$ junctions demonstrated a noticeably higher P. The relationship between R_{in} and P follows $P = V_{oc}I - R_{in}I^2$, where V_{oc} is the open-circuit voltage of the module. A peak power density (ω_{max}) of 0.45 W cm^{-2} was achieved under a temperature gradient (ΔT) of 294 K, which is slightly lower than the theoretical prediction (Figure 4b). In contrast, modules with Ni or 304SS as TEiMs exhibited only 65% and 80% of the ω_{max}, respectively, under the same ΔT.

Remarkably, the module utilizing Mg/$Mg_3(Bi,Sb)_2$ junctions achieved a maximum conversion efficiency (η_{max}) of 8.6% under

ΔT = 294 K, even after 30 days of aging (Figure 4c). Notably, no performance deterioration was observed compared to modules fabricated with unaged junctions (Figure S19, Supporting Information). In fact, a slight increase in efficiency was observed, likely due to enhanced electrical transport from Mg compensation and minor variations in the performance of the p-type junctions. The superiority of the $Mg/Mg_3(Bi,Sb)_2$ junctions is further evident in their η values compared to modules with conventional contact layers. As shown in Figure 4d, long-term thermal stability poses a significant challenge for $Mg_3(Bi,Sb)_2$ junctions. After aging, modules with $Ni/Mg_3(Bi,Sb)_2$ and $304SS/Mg_3(Bi,Sb)_2$ junctions exhibited significantly lower η of 6.6% and 7.1%, respectively.

To explore the potential for further performance enhancements, simulations were conducted to predict the module's η, incorporating the performance of the TE materials, the ρ_c of both n-type and p-type legs, and the properties of the TEiMs. Detailed simulation results are presented in Figure S20 (Supporting Information), showing that the simulated η_{max} could reach as high as 11.8%. Due to the inherent challenges in accurately measuring heat flow,[73] the experimentally measured Q_c tends to exceed the simulated values. To better illustrate the potential of our developed module, the η was recalculated using the measured P (P_m) and the simulated heat flow (Q_s). Under a ΔT of 294 K, the recalculated η_{max} reached an impressive 10.0% (Figure 4d). Compared to Bi_2Te_3-based and other $Mg_3(Bi,Sb)_2$-based modules (Figure 4e),[9,24,33,36,49,53,71,72] our module exhibits a superior ω_{max}, maintaining outstanding performance even after 30 days of aging. Notably, the experimentally realized η_{max} of 8.6% surpasses most previously reported two-pair modules designed for low-grade heat harvesting applications (ΔT < 300 K) (Figure 4f).[9,24,33,36,49,53,71,72] Moreover, the outstanding thermal stability of $Mg/Mg_3(Bi,Sb)_2$ junctions highlights their promise for long-term sustainable power generation. Looking ahead, the scalable fabrication of $Mg_3(Bi,Sb)_2$ materials remains a key challenge for real-world applications. Mechanical alloying and melting-sintering routes have shown promise for scaling up while preserving material performance.[74,75] Furthermore, the interfacial design developed in this work is compatible with industrial metallization techniques, such as chemical or electroplating, commonly used in Bi_2Te_3-based TE modules.[76] These factors highlight the feasibility of translating our findings toward practical module-level manufacturing.

3. Conclusion

To overcome the long-standing stability challenges at both the material and interface levels, we developed a holistically stable $Mg/Mg_3(Bi,Sb)_2$ junction by leveraging activated Mg diffusion. Introducing a Mg interlayer between $Mg_3(Bi,Sb)_2$ and the metallization layer not only ensures ultralow ρ_c but also preserves the intrinsic TE properties of the material, achieving unprecedented dual stability. The $Mg/Mg_3(Bi,Sb)_2$ junction maintains an ultralow ρ_c below 5 μΩ cm^2 while sustaining high σ of the material even after aging for over 100 days at 573 K. The Mg layer serves as a robust diffusion barrier while simultaneously compensating for Mg loss at grain boundaries, thereby enhancing electron transport within the TE material. This dual stability enables a remarkable η_{max} of 8.6% and ω_{max} of 0.45 W cm^{-2} under a ΔT of 294 K in a two-pair module, even after 30 days of aging of the n-type junctions. These findings highlight the exceptional potential of $Mg/Mg_3(Bi,Sb)_2$ junctions for sustainable power generation in low-grade heat harvesting applications. Moreover, the demonstrated dual stability in TE junctions provides valuable insights into achieving long-term reliability and enhanced performance in TE devices, paving the way for long-awaited practical and sustainable TE power generation applications.

4. Experimental Section

Materials Synthesis: To prepare the $Mg_{3.2}In_{0.02}Bi_{1.4}Sb_{0.595}Te_{0.005}$ (denoted as $Mg_3(Bi,Sb)_2$ in the main text), high-purity raw materials including Mg turnings (99.95%), Te shots (99.999%), Bi shots (99.999%), Sb shots (99.999%), and In powder (99.99%) were accurately weighed according to stoichiometry. The materials were loaded into a stainless-steel ball-milling jar inside an argon-filled glovebox. Ball milling was performed for 5 h in a single run using a SPEX 8000D high-energy mill. The resulting powder was consolidated by spark plasma sintering (SPS, SPS-1080 System, SPS SYNTEX INC) under pressure of 60 MPa at 973 K for 10 min. The p-type MgAgSb sample was prepared using a ball-milling process with the addition of 0.625 wt.% $C_{18}H_{36}O_2$. The obtained powder was consolidated by SPS at 573 K under 60 MPa for 5 min (SPS-322Lx, Dr. Sintering).

Properties and Microstructure Characterization: The electrical properties, including electrical conductivity (σ) and Seebeck coefficient (S), were measured using the ZEM-3 instrument in a helium atmosphere (ADVANCE RIKO, ± 5% uncertainty). The thermal conductivity κ was calculated using the equation $\kappa = \lambda C_p d$,where the thermal diffusivity λ was measured by a laser flash method (LFA 467, NETZSCH, ± 3% uncertainty), the densities d was measured by an Archimedes method. The heat capacity C_p was determined by the polynomial equation proposed by Agne et al.:[77] $C_p = 3NR\ (1 + 1.3 \times 10^{-4}\ T - 4 \times 10^3\ T^{-2})\ /\ M_w$, where N is the number of elements of the formula unit, M_w is the molecular weight of the formula unit. Microstructural and chemical compositions were characterized using a field-emission scanning electron microscope (FESEM, Hitachi SU8000) equipped with an energy dispersive spectrometer (EDS, XFlash FlatQUAD 5060F). Room-temperature contact resistance of the TE junctions was measured by a two-axis resistance distribution measurement instrument (S1331, Mottainai energy).

Module Fabrication and Efficiency Evaluation: To fabricate the $Ni/Mg/Mg_3(Bi,Sb)_2/Mg/Ni$ junction, Ni powder, Ni foil, Mg foil, and $Mg_3(Bi,Sb)_2$ bulk were loaded into a graphene die with a sandwich structure, followed by SPS at 773 K for 10 min. To minimize oxidation, freshly polished Mg foils were immediately transferred into an argon-filled glovebox for die assembly. Although the formation of a thin native MgO layer is difficult to completely avoid, it is not expected to significantly compromise the interfacial contact quality, as confirmed by low ρ_c and microstructural analysis. The $Ni/Mg_3(Bi,Sb)_2/Ni$ junction was fabricated using the same process, while the $304SS/Mg_3(Bi,Sb)_2/304SS$ junction was prepared by one-step SPS sintering under the same situation of material preparation. The obtained sandwich-structure legs were ground, polished and then cut into dice for module fabrication, with dimensions of 3.8 mm × 3.8 mm × 6 mm for both n-type and p-type legs. The prepared legs were placed inside quartz tubes and then evacuated for annealing in a muffle furnace. The Sb-based alloy was selected as the contact layer for preparing p-type legs by one-step SPS sintering. Two-pair modules were fabricated based on these n-type and p-type legs. The electrical output power and generation performance of the fabricated modules were characterized using a commercial apparatus (Mini-PEM, ADVANCE RIKO, Japan). The hot-side temperature (T_h) of the modules was controlled by a heater, and the cold-side temperature (T_c) was maintained by the flowing water. To characterize the performance of the TE junctions after aging, the junctions were re-soldered onto substrates. All modules were measured using the Mini-PEM system under identical operating conditions to ensure consistency. The 3D finite-element simulations of power-generation were performed with COMSOL Multiphysics®

software. The model incorporated the Heat Transfer in Solids, Electric Currents, and Thermoelectric Effect interfaces, which were fully coupled via the multiphysics node to capture the coupled thermal and electrical transport within the devices. The simulated geometry replicated the actual two-pair TE module constructed in this work. The hot-side temperature was varied from 373 to 593 K, while the cold side was fixed at 295 K. To simplify the model, thermal contact resistances at the interfaces was neglected. All material properties, including κ, S, and σ, were obtained from experimental measurements.

Supporting Information

Supporting Information is available from the Wiley Online Library or from the author.

Acknowledgements

L.W. A.L. and X.W. contribute equally to this work. We acknowledge financial support from the JST Mirai Program Grant Number JPMJMI19A1. Center support from JSPS WPI Academy is also thanked.

Conflict of Interest

T.M. and L.W. have filed one Japanese patent application (2025-017528) on the work described here. The remaining authors declare no competing interests.

Data Availability Statement

The data that support the findings of this study are available from the corresponding author upon reasonable request.

Keywords

elemental diffusion, interface engineering, $Mg_3(Bi, Sb)_2$, stability, thermoelectrics

Received: April 30, 2025
Revised: June 5, 2025
Published online: June 27, 2025

[1] Y. Zhou, T. Ding, G. Xu, S. Yang, C.-W. Qiu, J. He, G. W. Ho, *Nat. Rev. Phys.* **2024**, *6*, 769.
[2] J. D. Sachs, G. Schmidt-Traub, M. Mazzucato, D. Messner, N. Nakicenovic, J. Rockström, *Nat. Sustain.* **2019**, *2*, 805.
[3] G. Schierning, *Nat. Energy* **2018**, *3*, 92.
[4] G. J. Snyder, E. S. Toberer, *Nat. Mater.* **2008**, *7*, 105.
[5] T. Mori, S. Priya, *MRS Bull.* **2018**, *43*, 176.
[6] T. Hendricks, T. Caillat, T. Mori, *Energies* **2022**, *15*, 7307.
[7] W. Liu, S. Bai, *J. Materiomics* **2019**, *5*, 321.
[8] W. Liu, Q. Jie, H. S. Kim, Z. Ren, *Acta Mater.* **2015**, *87*, 357.
[9] L. Xie, L. Yin, Y. Yu, G. Peng, S. Song, P. Ying, S. Cai, Y. Sun, W. Shi, H. Wu, N. Qu, F. Guo, W. Cai, H. Wu, Q. Zhang, K. Nielsch, Z. Ren, Z. Liu, J. Sui, *Science* **2023**, *382*, 921.
[10] H. Tamaki, H. K. Sato, T. Kanno, *Adv. Mater.* **2016**, *28*, 10182.
[11] J. Zhang, L. Song, S. H. Pedersen, H. Yin, L. T. Hung, B. B. Iversen, *Nat. Commun.* **2017**, *8*, 13901.
[12] K. Imasato, S. D. Kang, G. J. Snyder, *Energy Environ. Sci.* **2019**, *12*, 965.
[13] J. Mao, H. Zhu, Z. Ding, Z. Liu, G. A. Gamage, G. Chen, Z. Ren, *Science* **2019**, *365*, 495.
[14] X. Shi, T. Zhao, X. Zhang, C. Sun, Z. Chen, S. Lin, W. Li, H. Gu, Y. Pei, *Adv. Mater.* **2019**, *31*, 1903387.
[15] R. Shu, Y. Zhou, Q. Wang, Z. Han, Y. Zhu, Y. Liu, Y. Chen, M. Gu, W. Xu, Y. Wang, W. Zhang, L. Huang, W. Liu, *Adv. Funct. Mater.* **2019**, *29*, 1807235.
[16] Z. Liu, N. Sato, W. Gao, K. Yubuta, N. Kawamoto, M. Mitome, K. Kurashima, Y. Owada, K. Nagase, C.-H. Lee, J. Yi, K. Tsuchiya, T. Mori, *Joule* **2021**, *5*, 1196.
[17] N. Chen, H. Zhu, G. Li, Z. Fan, X. Zhang, J. Yang, T. Lu, Q. Liu, X. Wu, Y. Yao, Y. Shi, H. Zhao, *Nat. Commun.* **2023**, *14*, 4932.
[18] J.-W. Li, Z. Han, J. Yu, H. L. Zhuang, H. Hu, B. Su, H. Li, Y. Jiang, L. Chen, W. Liu, Q. Zheng, J. F. Li, *Nat. Commun.* **2023**, *14*, 7428.
[19] J. Lei, K. Zhao, J. Liao, S. Yang, Z. Zhang, T. R. Wei, P. Qiu, M. Zhu, L. Chen, X. Shi, *Nat. Commun.* **2024**, *15*, 6588.
[20] P. Zhao, W. Xue, Y. Zhang, S. Zhi, X. Ma, J. Qiu, T. Zhang, S. Ye, H. Mu, J. Cheng, X. Wang, S. Hou, L. Zhao, G. Xie, F. Cao, X. Liu, J. Mao, Y. Fu, Y. Wang, Q. Zhang, *Nature* **2024**, *631*, 777.
[21] A. Li, Y. Wang, Y. Li, X. Yang, P. Nan, K. Liu, B. Ge, C. Fu, T. Zhu, *Nat. Commun.* **2024**, *15*, 5108.
[22] Y. Huang, J. Lei, H. Chen, Z. Zhou, H. Dong, S. Yang, H. Gao, T.-R. Wei, K. Zhao, X. Shi, *Acta Mater.* **2023**, *249*, 118847.
[23] L. Xie, J. Yang, Z. Liu, N. Qu, X. Dong, J. Zhu, W. Shi, H. Wu, G. Peng, F. Guo, Y. Zhang, W. Cai, H. Wu, H. Zhu, H. Zhao, Z. Liu, J. Sui, *Mater. Today* **2023**, *65*, 5.
[24] A. Li, L. Wang, J. Li, T. Mori, *Energy Environ. Sci.* **2024**, *17*, 8810.
[25] Z. Liu, J. Mao, J. Sui, Z. Ren, *Energy Environ. Sci.* **2018**, *11*, 23.
[26] Y. Wang, A. Li, Y. Hong, T. Deng, P. Deng, Y. Huang, K. Liu, J. Wang, C. Fu, T. Zhu, *Nat. Mater.* **2025**, https://doi.org/10.1038/s41563-024-02112-7.
[27] M. Liu, X. Zhang, S. Zhang, Y. Pei, *Nat. Commun.* **2024**, *15*, 6580.
[28] Q. Yang, S. Yang, P. Qiu, L. Peng, T.-R. Wei, Z. Zhang, X. Shi, L. Chen, *Science* **2022**, *377*, 854
[29] T. Cao, X. L. Shi, B. Hu, Q. Yang, W. Y. Lyu, S. Sun, L. C. Yin, Q. Y. Liu, W. Chen, X. Wang, S. Liu, M. Li, W. D. Liu, T. Tesfamichael, Q. Liu, J. MacLeod, Z. G. Chen, *Nat. Commun.* **2025**, *16*, 1555.
[30] L. Yin, X. Li, X. Bao, J. Cheng, C. Chen, Z. Zhang, X. Liu, F. Cao, J. Mao, Q. Zhang, *Nat. Commun.* **2024**, *15*, 1468.
[31] L. Miao, Q. Zhang, M. Yuan, R. Li, M. Wang, X. Tan, J. Wu, G. Q. Liu, J. Jiang, *Adv. Mater.* **2025**, 2503580.
[32] X. Wu, Z. Han, Y. Zhu, B. Deng, K. Zhu, C. Liu, F. Jiang, W. Liu, *Acta Mater.* **2022**, *226*, 117616.
[33] X. Wu, Y. Lin, Z. Han, H. Li, C. Liu, Y. Wang, P. Zhang, K. Zhu, F. Jiang, J. Huang, H. Fan, F. Cheng, B. Ge, W. Liu, *Adv. Energy Mater.* **2022**, *12*, 2203039.
[34] J. Chu, J. Huang, R. Liu, J. Liao, X. Xia, Q. Zhang, C. Wang, M. Gu, S. Bai, X. Shi, L. Chen, *Nat. Commun.* **2020**, *11*, 2723.
[35] R. Liu, Y. Xing, J. Liao, X. Xia, C. Wang, C. Zhu, F. Xu, Z. G. Chen, L. Chen, J. Huang, S. Bai, *Nat. Commun.* **2022**, *13*, 7738.
[36] Y. Fu, Q. Zhang, Z. Hu, M. Jiang, A. Huang, X. Ai, S. Wan, H. Reith, L. Wang, K. Nielsch, W. Jiang, *Energy Environ. Sci.* **2022**, *15*, 3265.
[37] Y. Fu, X. Ai, Z. Hu, S. Zhao, X. Lu, J. Huang, A. Huang, L. Wang, Q. Zhang, W. Jiang, *Nat. Commun.* **2024**, *15*, 9355.
[38] A. Li, L. Wang, J. Li, X. Wu, T. Mori, *Nat. Commun.* **2025**, *16*, 1502.
[39] L. Borgsmiller, D. Zavanelli, G. J. Snyder, *PRX Energy* **2022**, *1*, 022001.
[40] I. T. Witting, T. C. Chasapis, F. Ricci, M. Peters, N. A. Heinz, G. Hautier, G. J. Snyder, *Adv. Electron. Mater.* **2019**, *5*, 1800904.
[41] J. Male, M. T. Agne, A. Goyal, S. Anand, I. T. Witting, V. Stevanovic, G. J. Snyder, *Mater. Horiz.* **2019**, *6*, 1444.
[42] S. Ohno, K. Imasato, S. Anand, H. Tamaki, S. D. Kang, P. Gorai, H. K. Sato, E. S. Toberer, T. Kanno, G. J. Snyder, *Joule* **2018**, *2*, 141.
[43] S. Bano, R. Chetty, J. Babu, T. Mori, *Device* **2024**, *2*, 100408.

[44] A. Li, C. Fu, X. Zhao, T. Zhu, *Research* **2020**, *2020*, 1934848.
[45] H. Shang, Z. Liang, C. Xu, J. Mao, H. Gu, F. Ding, Z. Ren, *Research* **2020**, *2020*, 1219461.
[46] H. Cho, S. Y. Back, N. Sato, Z. Liu, W. Gao, L. Wang, H. D. Nguyen, N. Kawamoto, T. Mori, *Adv. Funct. Mater.* **2024**, *34*, 2407017.
[47] K. Yang, X. Li, C. Sun, W. Song, W. Zhao, Q. Zhang, *Adv. Funct. Mater.* **2024**, *34*, 2315886
[48] H. Yang, B. Jia, L. Xie, D. Mao, J. Xia, J. Yang, M. Yuan, Q. Gan, X. Liu, M. Hu, J. Shuai, J. He, *Joule* **2024**, *8*, 1.
[49] L. Wang, W. Zhang, S. Y. Back, N. Kawamoto, D. H. Nguyen, T. Mori, *Nat. Commun.* **2024**, *15*, 6800.
[50] A. Li, P. Nan, Y. Wang, Z. Gao, S. Zhang, Z. Han, X. Zhao, B. Ge, C. Fu, T. Zhu, *Acta Mater.* **2022**, *239*, 118301.
[51] J. Zhang, L. R. Jorgensen, L. Song, B. B. Iversen, *ACS Appl. Mater. Interfaces* **2022**, *14*, 31024.
[52] H. Shang, Z. Liang, C. Xu, S. Song, D. Huang, H. Gu, J. Mao, Z. Ren, F. Ding, *Acta Mater.* **2020**, *201*, 572.
[53] P. Ying, R. He, J. Mao, Q. Zhang, H. Reith, J. Sui, Z. Ren, K. Nielsch, G. Schierning, *Nat. Commun.* **2021**, *12*, 1121.
[54] Z. Bu, X. Zhang, Y. Hu, Z. Chen, S. Lin, W. Li, C. Xiao, Y. Pei, *Nat. Commun.* **2022**, *13*, 237.
[55] P. Ying, L. Wilkens, H. Reith, N. P. Rodriguez, X. Hong, Q. Lu, C. Hess, K. Nielsch, R. He, *Energy Environ. Sci.* **2022**, *15*, 2557.
[56] C. Xu, Z. Liang, W. Ren, S. Song, F. Zhang, Z. Ren, *Adv. Energy Mater.* **2022**, *12*, 2202392.
[57] L. Yin, C. Chen, F. Zhang, X. Li, F. Bai, Z. Zhang, X. Wang, J. Mao, F. Cao, X. Chen, J. Sui, X. Liu, Q. Zhang, *Acta Mater.* **2020**, *198*, 25.
[58] R. Chetty, J. Babu, T. Mori, *ACS Appl. Energy Mater.* **2024**, *7*, 12112.
[59] Y. Wang, J. Chen, Y. Jiang, M. Ferhat, S. Ohno, Z. A. Munir, W. Fan, S. Chen, *ACS Appl. Mater. Interfaces* **2022**, *14*, 33419.
[60] N. Qu, Y. Sun, Z. Liu, L. Xie, Y. Zhu, H. Wu, R. Chai, J. Cheng, F. Guo, Q. Zhang, R. Wang, B. Li, Z. Wei, W. Cai, J. Sui, *Adv. Energy Mater.* **2023**, *14*, 2302818
[61] J. Yang, G. Li, H. Zhu, N. Chen, T. Lu, J. Gao, L. Guo, J. Xiang, P. Sun, Y. Yao, R. Yang, H. Zhao, *Joule* **2022**, *6*, 193.
[62] L. Wang, A. Li, J. Li, N. Kawamoto, D. H. Nguyen, T. Mori, *Nano Energy* **2025**, *137*, 110797.
[63] E. D. l. Barrera, *Nat. Struct. Mol. Biol.* **2005**, *12*, 280.
[64] M. Liu, X. Zhang, J. Tang, Z. Chen, W. Li, Y. Pei, *Sci. Bull.* **2023**, *68*, 2536.
[65] T. V. Blank, Y. A. Gol'dberg, *Semiconductors* **2007**, *41*, 1263.
[66] S. M. Sze, K. K. Ng, *Physics of Semiconductor Devices*, John Wiley & Sons, Hoboken, NJ, USA **2006**.
[67] H. Sepehri-Amin, K. Imasato, M. Wood, J. J. Kuo, G. J. Snyder, *ACS Appl. Mater. Interfaces* **2022**, *14*, 37958.
[68] D. Li, F. Huang, B. Ren, S. Wang, W. Zhang, L. Zhu, *Sci. Rep.* **2024**, *14*, 905.
[69] Y. Geng, Z. Li, Z. Lin, Y. Liu, Q. Lai, X. Wu, L. Hu, F. Liu, Y. Yu, C. Zhang, *Small* **2023**, *20*, 2305670.
[70] J. J. Kuo, Y. Yu, S. D. Kang, O. Cojocaru-Mirédin, M. Wuttig, G. J. Snyder, *Adv. Mater. Interfaces* **2019**, *6*, 1900429.
[71] L. Yin, F. Yang, X. Bao, W. Xue, Z. Du, X. Wang, J. Cheng, H. Ji, J. Sui, X. Liu, Y. Wang, F. Cao, J. Mao, M. Li, Z. Ren, Q. Zhang, *Nat. Energy* **2023**, *8*, 665.
[72] M. Jiang, Y. Fu, Q. Zhang, Z. Hu, A. Huang, S. Wang, L. Wang, W. Jiang, *Natl. Sci. Rev.* **2023**, *10*, nwad095.
[73] R. Chetty, J. Babu, T. Mori, *Joule* **2024**, *8*, 556.
[74] Y. Liu, Y. Geng, Y. Dou, X. Wu, L. Hu, F. Liu, W. Ao, C. Zhang, *Small* **2023**, *19*, 2303840.
[75] Q. Zhang, M. Yuan, K. Pang, Y. Zhang, R. Wang, X. Tan, G. Wu, H. Hu, J. Wu, P. Sun, G. Q. Liu, J. Jiang, *Adv. Mater.* **2023**, *35*, 2300338.
[76] Q. Zhang, Q. Pan, M. Wang, K. Pang, R. Li, L. Miao, X. Tan, H. Hu, J. Wu, P. Sun, G.-Q. Liu, J. Jiang, *Acta Mater.* **2025**, *292*, 121064.
[77] M. T. Agne, K. Imasato, S. Anand, K. Lee, S. K. Bux, A. Zevalkink, A. J. E. Rettie, D. Y. Chung, M. G. Kanatzidis, G. J. Snyder, *Mater. Today Phys.* **2018**, *6*, 83.